Forced Atmospheric Teleconnections During 1979-2014

Tao Zhang[1,2], Martin P. Hoerling[2], Judith Perlwitz[1,2], and Taiyi Xu[1,2]

[1]Cooperative Institute for Research in Environmental Sciences

University of Colorado

Boulder, Colorado

[2]NOAA Earth System Research Laboratory

Physical Sciences Division

Boulder, Colorado

(*Submitted to Journal of Climate*)

March 23, 2015

Corresponding author address:

Dr. Tao Zhang

NOAA/ESRL/PSD

325 Broadway, R/PSD1

Boulder, CO 80305

Email: tao.zhang@noaa.gov

Abstract

Forced atmospheric teleconnections during 1979-2014 are examined using a 50-member ensemble of atmospheric general circulation model (AGCM) simulations subjected to observed variations in sea surface temperatures (SST), sea ice and carbon dioxide. Three primary modes of forced variability are identified using EOF analysis of the ensemble mean wintertime 500-hPa heights. The principal component time series of the first and second modes are highly correlated with Nino3.4 and Trans-Niño (TNI) SST indices, respectively, indicating their tropical sources. Their wintertime impacts are almost entirely confined to the Pacific-North American (PNA) sector. The leading mode describes the canonical atmospheric teleconnection associated with El Niño-Southern Oscillation (ENSO). The second mode describes a wavetrain resembling the classic PNA pattern that we show for the first time to be associated with distinctly different manifestations of tropical SST variability. In its positive polarity, this second mode is an expression of the asymmetry in atmospheric teleconnections between ENSO's extreme opposite phases. In its negative polarity, this second mode expresses the atmospheric sensitivity to a SST pattern resembling the precursor for subsequent El Niño development. Such a negative phase of the second forced mode was especially prominent during 2013-14 and explains key features of the California drought/heat wave.

The third mode, described by a hemisphere-scale increasing trend in heights, is related to radiatively forced climate change. We demonstrate that the observed trend of winter 500-hPa heights during the recent period is mostly unrelated to this radiatively forced mode, but is due largely to ENSO-like decadal variability.

1. Introduction

In their seminal study on atmospheric phenomena associated with the Southern Oscillation, Horel and Wallace (1981; hereafter HW) explored the linkage between tropical climate indicators and extratropical atmospheric circulation. A hypothesized pattern of upper troposphere height anomalies during episodes of warm equatorial Pacific sea surface temperatures (SSTs) described a wave train arching northward from the central Pacific and eastward across North America. Using global reanalysis data not available at the time of the HW study, Fig. 1 (top) shows Northern Hemisphere features of such a pattern possessing the essential characteristics first hypothesized by HW. The analysis is based on regressing a wintertime index of Nino3.4 SSTs onto NCEP/NCAR reanalysis (Kalnay et al. 1996) 500 hPa heights for the 1951-78 core study period used in HW, with the phase depicting conditions during warm (El Niño) SST events. Confirmation that tropical SSTs in fact force a pattern bearing the essential shape, scale, and seasonality described in HW was provided by dynamical model studies (e.g. Hoskins and Karoly 1981; Simmons 1982; Simmons et al. 1983), and by the results of numerous subsequent general circulation model experiments. This atmospheric circulation pattern is now commonly referred to as the El Niño/Southern Oscillation (ENSO) teleconnection to denote the long-distance tropical ocean forcing of extratropical seasonal climate.

Is this the only atmospheric circulation pattern forced by SSTs during boreal winter, and is it even the most dominant forced pattern? As first posed by HW, who wondered whether the ENSO teleconnection pattern that they conceived from analysis of a few historical El Niño cases represented a "*blurred image resulting from our inadvertent*

superposition of an ensemble of sharper images, corresponding to the various states of the equatorial atmosphere under the general category of warm episodes", the principal goal of our study is to address this classic problem of seasonal climate variability.

Shortly after the HW study, nature offered an experiment that addressed this question, generating in 1982-83 what was then estimated to be the strongest El Niño of the century (Cane 1983). In reviewing the meteorological aspects of that event, Rasmusson and Wallace (1983) contrasted the atmospheric circulation originally estimated from a composite of past events in HW with the specific conditions during winter 1982-83. While resembling some of the features seen in Fig. 1a, the authors noted that the anticyclonic conditions over Canada were shifted eastward, as was the North Pacific low pressure during 1982-83. North American surface conditions were also appreciably different than those of the historical composite, including mild winter temperatures over southern Canada and the eastern U.S. and extremely wet and stormy conditions over California and the Southwest U.S.

Were the particular conditions of 1982-83 an example of the atmosphere's sensitivity to unique SST forcing of that winter? A second very strong El Niño event occurred during 1997-98 whose attending atmospheric circulations and North American climate conditions bore considerable resemblance to those observed in 1982-83 (e.g. Hoerling and Kumar 1997; Kang et al. 2002). It is therefore plausible that differences between the ENSO teleconnection inferred from regressions on Nino3.4 SST during 1951-1978 (Fig. 1, top) and those inferred from data during 1979-2014 (Fig. 1, bottom) is due to different

response patterns associated with very strong SST forcing events in the decades after HW.

Posed in the context of seasonal climate prediction, the issue is whether different North American wintertime conditions during El Niños can be anticipated on the basis of particular characteristics of the SST forcing. To tackle the question of whether ENSO could be used as predictor for seasonal climate, but especially to assess the relevance of ENSO diversity, numerous groups have conducted atmospheric general circulation model (AGCM) experiments over the last 30 years. Early experiments produced conflicting results, with Geisler et al. (1985) finding a single geographically fixed pattern of NH response to different patterns and magnitudes of warm tropical Pacific SSTs, and Palmer and Mansfield (1986b) finding the 1982-83 El Niño forcing to induce a different atmospheric response than that associated with composite El Niño forcing. A strong dependency of responses upon the quality of a model's climatology was shown to exist (e.g. Palmer and Mansfield 1986a), and early results using coarse resolution climate models, often performed in idealized perpetual January mode, need to be interpreted with great caution.

Another limitation that has plagued most modeling studies to date is the small ensemble sizes available from which to reliably extract the atmospheric responses for individual events. Thus, while Hoerling and Kumar (2000) found observed inter-El Niño variability in atmospheric circulation to be mostly unrelated to event-to-event differences in SSTs, the strength of their conclusion was undermined by their reliance on a relatively small 12-

member ensemble. In a subsequent study, Hoerling and Kumar (2002) attempted to overcome the sampling problem by pooling simulations across four different models. The analysis of that multi-model ensemble revealed different response patterns depending on the characteristics of the tropical SST forcing, though much of the ENSO response manifested as a single spatial pattern. Whereas the larger ensemble size was evidently important for detecting additional atmospheric response patterns, the use of a multi-model approach introduced a new uncertainty in the interpretation. Recalling the lessons from early AGCM intercomparisons that revealed substantial model dependency in atmospheric responses, the possibility existed that the additional patterns found in Hoerling and Kumar (2002) were not signatures of a robust sensitivity. Furthermore, similar to the problem of potentially blurring sharper images of atmospheric responses to ENSO when constructing an observed composite, the process of multi-model averaging may likewise obscure such patterns.

To overcome these limitations, Kumar et al. (2005) diagnosed an 80-member ensemble of AGCM historical runs using a single model. Their approach took advantage of a lagged ensemble of hindcast experiments that were being routinely conducted as part of the National Centers for Environmental Prediction (NCEP) seasonal forecast system. Applying empirical orthogonal function (EOF) analysis to the ensemble mean as in Hoerling and Kumar (2002), they found a leading atmospheric response pattern bearing considerable resemblance to the HW teleconnection, but importantly explaining only about half of the magnitude in overall wintertime SST forced variability. The second response pattern exhibited strong zonal symmetry, whose time series was a trend during

the 1980-2000 study period. A third pattern again revealed strong regional variability, resembling some features of the third EOF pattern in Hoerling and Kumar (2002).

In sum, the two large ensemble model studies on SST-forced wintertime atmospheric circulations---one from a multi-model approach and a second from a particular model---indicate that the HW hypothesized teleconnection pattern is indeed a robust and a dominant structure of the atmospheric circulation sensitivity to SST variability. To zero-order, the magnitude and phase of this pattern can be understood to vary linearly with the magnitude and phase of ENSO-related tropical Pacific variations. This view of the atmospheric sensitivity appears to account for roughly half of the wintertime NH variability in *SST forced circulation variability*, though a greater portion over select regions such as the central North Pacific. The high-order patterns are less well understood, and currently lack clear physical interpretation. For instance, the third leading pattern has been argued to be linked to SST-driven teleconenctions during non-ENSO years in Hoerling and Kumar (2002), while a similar pattern in Kumar et al. (2005) was believed to result form the nonlinear atmospheric response to extreme opposite phases of ENSO. Also unresolved is the physical explanation for a more zonally symmetric response pattern that appears to be emergent in the time series of the forced solutions.

In so far as prior analyses have ended in either 1999 or 2000, it is important to update the study to include a period in which external radiative forcing of climate has led to a detectable effects on sea surface temperatures (IPCC 2013), though effects on

atmospheric circulation remain unclear. Further, it is important to understand whether the dominant ENSO-related teleconnection pattern has changed during this period of anthropogenic climate change. In particular, is the difference between the two teleconnections of Fig. 1 attributable to such emergent forcing, or is it perhaps a symptom of different ENSO statistics in the recent decades?

This study utilizes large ensemble sized AGCM and coupled atmosphere-ocean model simulations to examine forced atmospheric teleconnections over the recent period (1979-2014). Specifically, it addresses the question of whether there is more than one SST forced mode of extratropical Northern Hemisphere circulation variability during this period, and if so, what are their physical interpretations.

The model and analysis methods are described in Section 2. Conducting a parallel diagnosis of a different AGCM assesses robustness of the results. Section 3 then focuses on a physical interpretation of the December-February atmospheric sensitivity to SST variability in GFS for the period 1979-2014. A summary and concluding remarks appear in Section 4.

2. Data and Methods

a. Observed and model data

The characteristics of atmospheric variability are diagnosed from analysis of 500 hPa geopotential height fields conducted over the region 20°N-90°N. The study is of the Northern Hemisphere (NH) December-January-February (DJF) winter season and

focuses on the recent 1979-2014 period. Estimates of the observed variability are derived from the National Centers for Environmental Prediction (NCEP)–National Center for Atmospheric Research (NCAR) reanalysis product [*Kalnay et al.* 1996].

In order to determine the physical factors responsible for the observed 500 hPa height variability, we utilize atmospheric models (also called Atmospheric Model Intercomparison Project (AMIP) experiments) and coupled ocean-atmospheric models (also called Coupled Model Intercomparison Project (CMIP) experiments). For the former, the study primarily uses the National Centers for Environmental Prediction (NCEP) Global Forecast System model version 2 (GFSv2), the atmospheric component of the Climate Forecast System (CFS) version 2 (*Saha et al*. 2014). The model is run at T126 horizontal resolution with 64 vertical levels, and forced with specified observed monthly varying sea surface temperatures, sea ice (Hurrell et al. 2008), and carbon dioxide concentrations for 1979-2014. Climatological values are specified for other greenhouse gases (e.g. CH4, NO2, O3, CFCs), aerosols, solar, and volcanic aerosols. A 50-member ensemble is conducted, each member forced identically but differing only by its initial atmospheric condition. The time evolving forced signal is derived from analysis of the 50-member ensemble average. To assess the robustness of key features in the GFS forced responses, we also diagnosis the time evolving signal from an 85-member ensemble of the European Center-Hamburg Max Planck Institute for Meteorology model 4.5 (ECHAM4.5; Roeckner et al. 1996) that spans January 1950 through February 2003. The model was run at T42 horizontal resolution with 19 vertical levels.

The signal in these AMIP experiments is further diagnosed to assess the component linked to changes in external radiative forcing, which may affect variability in 500 hPa heights through its influence on lower boundary conditions such as SSTs and sea ice (e.g. related to the ocean's response to long term global warming) and through direct atmospheric effects of changes in radiative forcing. To isolate the role of the external radiative forcing alone, we use a multi-model, 50-member ensemble of historical CMIP simulations. A 20-member ensemble is based on the Community Climate System Model, version 4 (CCSM4; Gent et al. 2011) whose atmospheric component is Community Atmospheric Model version 4 (CAM4; Neale et al. 2010), and a 30-member ensemble (Kay et al. 2015) is based on the Community Earth System Model version 1 (CESM1; Meehl et al. 2013) whose atmospheric component is CAM5 (Neale et al. 2012). Both atmospheric components are run at ~1° horizontal resolution, with 26 vertical levels in CAM4 and 30 levels in CAM5. Each member of these two coupled model runs is identically driven by changes in greenhouse gases, anthropogenic aerosols, solar and volcanic aerosols, with starting from different initial conditions. The radiatively forced atmospheric signals are derived from the ensemble-mean of 50 coupled runs, in order to effectively separate the atmospheric response pattern from those arising from unforced internal coupled ocean-atmospheric variability alone.

b. Diagnostic methods

The observed leading structures of the NH wintertime circulation patterns are obtained by applying empirical orthogonal function (EOF) analysis to DJF seasonally averaged 500-

hPa heights for the 35 years of data during 1979-2014 period. The EOF analysis is based on the covariance matrix for 20°N-90°N latitude bands, and a latitudinal weighting prior to the EOF analysis is used. The EOF patterns are presented as regressions against the principal component (PC) time series.

In Appendix A, we provide a comparison of the patterns of the observed and GFS simulated first three leading modes of variability of DJF 500 hPa geopotential heights. This comparison demonstrates that the model is capable of capturing the observed two leading modes of variability when concatenating the individual members of the GFS AMIP simulations. These modes can also be largely reproduced in a long control run with climatological lower boundary conditions, suggesting that the internal atmospheric variability may play a dominant role in Northern Hemisphere wintertime height variability. Section 3 will present the analysis of the fraction of the forced atmospheric variability versus the total wintertime height variability to further quantify the role of the internal atmospheric variability.

In addition, EOFs are calculated of the ensemble mean 500 hPa heights of the AMIP and the CMIP data. For the former model suite, the resulting patterns are of the atmospheric sensitivity to the specified SST, sea ice, and radiatively forcing during 1979-2014. These forcings commingle both internal variations (e.g., ENSO) and external variations related to anthropogenic climate change. For the latter model suite, the resulting patterns are of the atmospheric sensitivity to specified radiative forcing alone. While the coupled models produce internal ocean variations such as ENSO, these are not temporally

coherent among the individual ensemble members in the manner that they are (by specification) in AMIP experiments. Thus, any SST-forced component of height variability in the CMIP analysis will be principally related to the trend component of global SST change that is coherent with the time series of radiative forcing.

Finally, composite analyses of 500-hPa height for extreme phases of the EOF patterns are diagnosed, and the associated patterns of sea surface temperatures, and North American surface air temperature and precipitation are analyzed.

3. Results

a. Principal time-varying forced signals

Figure 2 shows wintertime (DJF) 500 hPa height structures based on the two leading EOFs of the ensemble-averaged AMIP simulations. Together these explain 79% of the total boundary forced height variance. Contours in the left panels are the ensemble-mean 500 hPa heights regressed against each eigenvector's PC time series shown in the right panels for 1979-2014.

A wave train having principal centers over the Pacific-North American sector describes the height pattern maximizing variance in the extratropical NH forced solutions. Its structure is well-known, resembling the observed height anomalies that are linearly related to Nino3.4 SST variability (see Figure 1) and also resembling the configuration related to the leading EOFs of wintertime heights in both observations and model (see Figure A1). The time series for this leading mode shows clear co-variability with ENSO,

having positive polarity (i.e., the phase as shown in Fig. 2) during warm events (e.g. 1982/83, 1991/92, 1997/98, 2002/03, 2009/10) and negative polarity (i.e., the opposite phase to that shown in Fig. 2) during cold events (e.g. 1988/89, 1998/99, 1999/2000, 2007/08, 2011/12). This pattern alone explains 56% of total boundary forced component of extratropical NH wintertime height variability.

The height pattern associated with the second mode of forced AMIP solutions also describes a wave pattern confined mostly to the PNA sector. Explaining 23% of the total boundary forced height variability over the NH extratropics, its centers-of-action are in spatial quadrature with the leading forced solution. This pattern arises from several configurations of tropical Pacific SST variability. During strong El Niño warm events, both PC1 and PC2 have large values, with the second EOF pattern acting to modify the overall forced response by effectively shifting the centers-of-action of the first EOF pattern eastward. In this sense, various magnitudes of PC1 and PC2 during warm events describe so-called "flavors of El Niño". The second EOF also describes the asymmetry in teleconnections between El Niño and La Niña events, and is thus the spatial manifestation of the nonlinearity in atmosphere responses to ENSO's opposite phases. Finally, this pattern can arise in the absence of ENSO, being the dominant forced solution at times when NINO3.4 SSTs are "ENSO-neutral". Thus, while the stronger amplitudes in the corresponding PC-2 time series (Fig. 2, lower right) tend to occur during ENSO events (e.g. 1982/83, 1991/92, 1997/98 warm events, and 1988/89, 1998/99, 2007/08, 2010/11, 2011/12 cold events), large projections also occur during several ENSO-neutral years (1985/86, 1996/97, 2001/02, 2013/14). At such times, the forced solution is

materially different from the canonical ENSO teleconnection and has different impacts on North American surface temperature and precipitation than the canonical ENSO signals, as described further in section 3b.

We have utilized the large ensemble AMIP simulation from a different atmospheric circulation model to repeat the analysis and found that the results are robust (Appendix B). This Intercomparison indicates that the atmospheric sensitivities are unique to the nature of the boundary forcing to which each atmospheric model was subjected, rather than depending on the selection of a particular model. Our subsequent analysis is thus based on the GFS data.

We diagnose the scatter relationship between the PC indices shown in Figure 2 and various tropical Pacific SST indices to better understand the linkage between the first two EOF modes and oceanic forcing during 1979-2014. The top panel of Fig. 3 shows the relationship between the Nino3.4 standardized SST index, which is commonly used to monitor ENSO, and the PC time series for the EOF1 500 hPa height mode (PC1). The bottom panel of Fig. 3 shows the relationship between the Trans-Niño standardized SST index (TNI), which measures the contrast in SSTs across the equatorial Pacific and helps to capture the evolution of ENSO during its transition period (Trenberth and Stepaniak 2001), and the PC time series for the EOF2 500 hPa height model (PC2). The correlation between PC1 and Nino3.4 indices is 0.90, confirming that the height pattern associated with the leading mode of forced AMIP solutions is the atmospheric expression of ENSO forcing; the so-called canonical ENSO teleconnection. The correlation between PC2

index and TNI index is also high (0.74), indicating that the height pattern associated with the second mode of forced AMIP solutions is linked to the evolution of ENSO.

Whereas the overall temporal correlation between the PC1 and PC2 time series is zero, there is nonetheless a strong physical relationship between these two as mentioned previously. To explore the connection between PC1 index and PC2 index, Figure 4 shows the scatter relationship between them. While there is no linear correlation between these two PC time series by statistical construct, a nonlinear relationship is evident. For the extremes values of PC1, PC2 is always positive. Further, the extreme positive occurrences of PC2 arise solely in concert with strong PC1 states. Recalling that the latter is a proxy for NINO3.4 SST variability, this result illustrates the nonlinearity of atmospheric teleconnections through which the second response pattern is of the same phase during both strong El Niño and La Niña events. This non-linear relation between the PC1 and PC2 circulation patterns is mirrored by a similar non-linear relation between the two leading EOF modes of tropical Pacific SSTs (Dommenget et al. 2013), with those SST patterns being well described by the NINO34 and TNI indices, respectively. Affirmed hereby is that the difference between the oceanic expressions of El Niño and La Niña events is responsible for a difference in atmospheric teleconnections between ENSO's extreme states.

An interesting feature of the scatter relation is that the strong negative phases of PC2 occur almost exclusively when PC1 is near-normal, namely only during ENSO-neutral conditions. The result isolates the existence of a forced atmospheric teleconnection that

is distinct from the well-known teleconnection occurring during mature ENSO conditions. The forced atmospheric circulation described by this PC2 is thus not a mere modifier of the canonical ENSO patterns, but can also exist as a unique stand-alone sensitivity pattern given particular states of the tropical ocean. As will be subsequently shown in composite analyses, this wintertime teleconnection emerges in the interlude between tropical SST evolutions from a recently completed La Niña to a subsequent El Niño. Within this transition toward El Niño, warm SSTs are often present in the tropical west Pacific and cool conditions are lingering in the tropical east Pacific, a pattern resembling the optimal structure for El Niño development 6-9 month later (Penland and Sardeshmukh 1995). These results indicate that there is a distinct atmospheric teleconnection (the negative phase of PC2) that accompanies such a precursor state to El Niño development.

b. Composite forced signals

Various characteristics of wintertime global climate associated with the leading forced atmospheric teleconnection are illustrated in Fig. 5. Shown are the composite patterns of Northern Hemisphere 500-hPa height, tropical SST and precipitation, North American surface temperature, and North American precipitation based on the upper and lower quintile of the PC1 time series during 1979-2014. Each composite consists of a 350-wintertime average constructed from the 7 strongest cases averaged across the 50-member model simulation.

For positive PC1 (Fig. 5, left), tropospheric circulation anomalies (top panel) resemble the Tropical/Northern Hemisphere (TNH) pattern (Mo and Livezey 1986). This positive

phase occurs in concert with warm equatorial Pacific SSTs during the mature phase of El Niño (second panel). The well-known southeastward shift of low pressure from the Aleutians into the Gulf of Alaska and a development of anomalously high pressure over central Canada are part of a hemispheric wave train that brings above-normal temperatures to central and eastern North America (third panel) and above-normal rainfall to the southwestern United States (bottom panel). For negative PC1 values (Fig. 5, right), the global climate conditions are almost a mirror image, affirming the dominant linearity in atmospheric response to the extreme values of the Nino3.4 index. Some asymmetries are evident, however. For instance, the 500 hPa height anomaly centers are shifted 20-30° longitude west in the PC1 negative composite compared to PC1 positive composite, and resemble the Pacific-North American circulation pattern (Barnston and Livezey 1987) rather than the TNH pattern. Such asymmetry in the model's response is consistent with observational evidence of nonlinearity in atmospheric teleconnections associated with El Niño and La Niña (e.g. Hoerling et al. 1997).

The asymmetry in global climate conditions between extreme phases of PC1 is diagnosed in Fig. 6, which presents the sum of composite anomalies for extreme positive PC1 (left panels, Figure 5) and negative PC1 (right panels, Figure 5). The asymmetric height pattern (top) is symptomatic of the aforementioned phase shift in teleconnections, a structure very similar to the second EOF pattern of forced atmospheric teleconnections (see Fig. 2). Consistent with the scatter relation of PC1 and PC2 time series, this result again demonstrates a physical relationship between the two leading EOFs of forced circulation, even though their respective time series are uncorrelated.

It is principally the difference in tropical forcing distinguishing strong El Niño from strong La Niña events that causes the asymmetry in teleconnections related to PC1 (e.g. Hoerling et al. 2001). Strong El Niños acquire larger SST amplitudes in the eastern equatorial Pacific whereas strong La Niñas acquire larger SST amplitudes in the western equatorial Pacific (Dommenget et al. 2013), the signature of which is captured in Fig. 6 (second panel). The resulting positive skew in the Nino3 index is further indication for nonlinearity in SST forcing (Burgers and Stephenson 1999; An and Jin 2004; Zhang et al. 2009; Zhang and Sun 2014). Tropical convection is sensitive to such differences, with strong El Niños exhibiting more enhanced rainfall in the eastern Pacific, whereas strong La Niñas have more suppressed rainfall in the western Pacific. As will be subsequently shown, this dipole in tropical forcing is not solely a residual of ENSO variance, but also arises during non-ENSO winters when the tropics can likewise act to force a teleconnection pattern resembling PC2.

The asymmetric component of US climate conditions is physically consistent with those expected from the circulation asymmetry, the physical linkages of which have been examined in detail in Zhang et al. (2014). Here we add the interpretation that the skew in ENSO SST distributions implants a tendency toward non-Gaussian statistics in North American surface temperature. Over eastern North America especially, an outcome of asymmetry in the tropically forced teleconnection is that warm conditions, which appear during both strong El Niño and La Niña, would occur with greater frequency than expected from assumptions of normality (see Fig. 6, third panel). The asymmetric

component of precipitation (Fig. 6, bottom) has a somewhat different interpretation. The widespread wet conditions over the West Coast result from the fact that the strong El Niño wet signal in central-northern California is appreciably more intense than the La Niña dry signal. Further, strong El Niños do not yield substantial wintertime dryness over Oregon/Washington, whereas those areas are considerably wet during La Niña. Overall, these indications for asymmetry in US climate impacts, originating from teleconnections driven by ENSO extremes, reveal a rectified effect comprised of a wetter far western North America and a warmer eastern North America, than would prevail in a climate lacking extreme ENSO variability.

Figure 7 presents the various characteristics of wintertime global climate associated with the second EOF of forced atmospheric teleconnection. Noteworthy here is that the composite maps for positive PC2 (left panels) are virtually identical to those associated with the asymmetric component of PC1 (cf. Figure 6). This follows directly from the scatter relation of the two PC time series (Fig. 4) where it was shown that most of the extreme positive states of PC2 occur in concert with the extreme PC1 positive and negative states. Thus, the simulation years comprising the composite of 7 extreme positive PC2 events, used to construct the left panels in Fig. 7, consist of a sum of extreme positive and negative PC1 cases from which the results of Fig. 6 were constructed. Physically, this positive PC2 phase and its associated global climate conditions are principally linked to ENSO.

On the other hand, the composite maps for negative PC2 (Fig. 7, right panels) are identified with SST forcing that is distinct from the mature states of ENSO. This phase of the teleconnection, consisting of anomalous low pressure over the central Pacific and anomalous high pressure along western North America, occurs in association with warm equatorial SST anomalies located slightly west of the Dateline, and cold SST anomalies along the equatorial east Pacific. The structure and phase of this teleconnection can be physically understood as resulting from tropospheric wave driving by enhanced convection initiated over the warm waters of the western Pacific, as demonstrated in dynamical model studies (e.g. Ting and Sardeshmukh 1993) and in idealized SST-driven climate simulations (Hoerling and Kumar 2002). The SST pattern is analogous to a pattern that is the precursor to El Niño development (e.g. Penland and Sardeshmukh, 1995). The principal North American impact of this pattern is dry/warm across the western United States.

An application of this result concerning PC2 is that it clarifies and supports recent interpretations on causes for California drought in 2013-14, in particular the possible role of tropical forcing (e.g. Wang et al. 2014; Seager et al, 2014). We note that the largest negative PC2 loading since 1979 occurred during the 2013-14 winter (see Fig. 2) indicating that this non-ENSO, tropically forced teleconnection was a candidate mechanism in the severe drought and heat over California and the Far West. The results of AMIP simulations using 7 different climate models also have found a wave pattern of the type described by this negative phase of PC2 during winter 2013-14 (Seager et al. 2014)

c. Radiatively forced time-varying atmospheric signals and trends

Results in the previous sections indicate that the two leading forced teleconnections are strongly linked to interannual states of tropical Pacific SST forcing, either mature ENSO conditions or pre-cursor conditions preceding El Niño development. The PC1 time series also exhibits a downward trend during 1979-2014 (see Fig. 2), which may reflect an increased frequency of cold ENSO states in the recent decade compared to the first decade, or may be suggestive of other low frequency forcing. The question arises in particular whether the trend in this leading teleconnection during 1979-2014, or trends in other manifestations of the model's forced responses, is symptomatic of atmospheric sensitivity to time variations in external radiative forcing.

To address this question, we begin by diagnosing the third EOF of the AMIP ensemble mean 500 hPa wintertime height variability (Fig. 8, top left). While explaining only 6% of the variance in forced height variability (the first two EOFs explain 80% of the variance), its pattern and temporal variability permit plausible physical interpretation in a framework of global warming. First, EOF3 primarily describes a monopole structure over the NH as a whole, a hemisphere-wide pattern distinct from the regional wave structures of EOF1 and EOF2 that were each confined to the Pacific-North American sector. Second, the PC3 time series (Fig. 8, top right) has a distinct upward trend that describes a tendency for NH heights to rise since 1979 as would be expected from the effects of anthropogenic greenhouse gas forcing.

Salient features of this third AMIP pattern also describe the leading pattern of CMIP solutions, thereby further supporting an interpretation that it is consistent with a sensitivity to time varying radiative forcing. Shown in the lower panel of Fig. 8 is EOF1 of a 50-member ensemble of CMIP simulations. Recall that the only forcing that is temporally synchronized among every CMIP model realization is anthropogenic greenhouse gases, anthropogenic aerosols, solar and volcanic variability. The leading 500 hPa height pattern associated with such forcing describes a hemisphere-wide monopole whose time series consists of an upward trend. These characteristics reproduce many features of the space-time variability of EOF3 from the AMIP analysis, including also the magnitude of variations, which are typically about 5 meters in both.

The results, from several lines of evidence, thus indicate radiative forcing to be instrumental in understanding the third EOF of AMIP responses. To the point of our earlier question, the results also indicate that a trend in the leading EOF of AMIP responses is unlikely a symptom of sensitivity to time variations in external radiative forcing.

How large is the contribution of radiative forcing changes to the total circulation variability during 1979-2014? To address this question, Figure 9 presents the ratio of wintertime 500 hPa height variances calculated for the AMIP (top) and CMIP (bottom) simulations. The total variance, which appears in the denominator of the ratio, commingles forced variations and internally driven variations (either of the atmosphere alone in AMIP or of the coupled ocean-atmosphere in CMIP). Its magnitude and spatial

pattern is very similar in the two model configurations (not shown). The forced components, which appear in the numerator of the ratio, are very different however. The forced component in CMIP represents the physical effects of external radiative forcing arising from both the atmosphere's sensitivity to lower boundary changes (e.g., a broad oceanic warming in response to increasing radiative forcing), and the direct effects of radiative forcing on the atmosphere alone. As shown in the lower panels of Fig. 9, this forced component is a small fraction of total variability, generally less than 5% poleward of 30°N. A similar pattern of variance ratios is found when using the AMIP EOF3 forced signal in the numerator (Figure 10), thus providing further evidence that radiative forcing is unlikely to be a substantial factor in driving variability of wintertime extratropical circulation.

The results support the interpretation that radiative forcing has limited explanatory power for height variations during 1979-2014. As a consequence, knowledge of the time series of radiative forcing offers little potential for predicting the overall variability in wintertime atmospheric circulation.

By contrast, the forced component in AMIP incorporates the atmosphere's sensitivity to the particular history of observed ocean variability, including especially ENSO variations observed during 1979-2014, in addition to the aforementioned physical effects related to radiative forcing. Strong atmospheric forcing by the particular history of SST variations explains why the ratio of variances in the AMIP simulation, shown in the upper panels of Fig. 9, is much larger than in CMIP. The magnitude is nearly an order of magnitude

greater in portions of the Pacific-North American region in AMIP versus CMIP. It is in that region especially where atmospheric responses to observed tropical Pacific SST variations that occurred during 1979-2014 dominates the overall boundary forced variance in AMIP.

The results of the AMIP analysis thus indicate the particular history of tropical Pacific SST variability to be key for understanding the nature of forced atmospheric teleconnections during 1979-2014. These SST forcings render appreciable explanatory power for PNA-sector height variations, and knowledge of the time series of ENSO and related internal states of the tropical Pacific Ocean offers substantial potential atmospheric predictability, whereas the radiative forcing alone explains little variance. The same distinction does not hold elsewhere. Both AMIP and CMIP variance ratios are small over the North Atlantic, Europe, or Asia. In those regions, the results of Fig. 9 indicate that neither radiative forcing alone, nor the additional knowledge of the sequence of observed SST variations, contributes appreciably to circulation variability thereby limiting overall predictability.

Figure 11 reveals that it is principally EOF1, and not EOF3, that explains most of wintertime NH 500 hPa height trend occurring in the AMIP ensemble. The left panels of Fig. 11 compare the 1979-2014 trend in 500 hPa heights associated with EOF1 (top) to the total AMIP ensemble mean trend (bottom). These are almost indistinguishable in pattern and magnitude indicating that irregularity in Nino3.4 SST variability during this period, with greater frequency of La Niña events in later years, is mainly responsible for

trend in forced circulations. Incorporating the trend contribution from EOF3 doesn't materially change the trend derived from EOF1 alone (see Fig 11, top right). Most of the regional patterns of NH wintertime height change since 1979 are thus unrelated to the radiative forcing time series, consistent with the findings of Perlwitz et al. (2015).

It is instructive to compare the AMIP ensemble mean height change since 1979 with the observed height change pattern. Agreement is strong, principally over the North Pacific where both indicate trends toward increased anticyclonic circulation (compare bottom panels of Fig. 11). The agreement over the North Pacific is not surprising given the high signal-to–noise ratio for interannual variability found in the AMIP simulations (Fig. 9) Physically, this observed trend toward anticyclonic circulation is consistent with atmospheric sensitivity to a change in ENSO statistics, with La Niña events more common during 1999-2014 while El Niños dominated the 1980s and 1990s. The ratio of variance indicates that detectability of such a North Pacific circulation change in observations is expected to be high, and thus the fidelity of the simulated trend is not surprising. The interpretation is not particularly dependent on whether one interprets the change in Pacific basin SSTs during 1979-2014 as symptomatic of ENSO-like interdecadal variability (e.g. Zhang et al. 1997), or indicative of a Pacific decadal climate oscillation (e.g. Mantua et al. 1997). By contrast, an observed circulation trend over the North Atlantic basin, which projects onto a negative phase of the North Atlantic Oscillation (NAO), is not reconcilable with forcing in the AMIP (or CMIP) simulations. Here the ratio of variances analysis showed forcing to be ineffective in driving interannual variability of atmospheric circulation, and it is plausible that the recent trend

toward the negative NAO phase is largely a symptom of internal atmospheric variability (see also Perlwitz et al. 2015).

4. Summary and Discussion

In this study, the forced modes of NH winter 500-hPa heights for the period of 1979 to 2014 were determined by utilizing a 50-member ensemble of atmospheric general circulation model (AGCM) simulations and by carrying out an EOF decomposition of the ensemble mean 500-hPa height anomalies. We identified three main modes that together explain about 85% of the forced variability of 500 hPa wintertime height variability poleward of 20°N.

The first two leading modes, which together explain 79% of the forced height variance, are associated with tropical SST forcing. The first EOF describes the canonical tropical-extratropical teleconnection pattern that has historically been interpreted as the linear response to ENSO's extreme opposite phases. That is, the positive (negative) phase (indicated by PC values) of the first EOF mode is linked to the response during warm (cold) ENSO events. A high correlation (~0.9) between the principal component of this EOF and the Nino3.4 index therefore exists. The second forced mode is closely linked to the Trans-Nino index—a correlation coefficient of 0.74 is found between the TNI and the principal component time series of this mode.

Our analysis of the scatter relationship between the PCs of these first and second modes, together with composite analyses, offers new insights into the physics of this second forced teleconnection pattern. Its positive phase is shown to be an expression of the asymmetry in ENSO teleconnections between its extreme opposite warm and cold phases. We thus interpret the second mode of forced teleconnection to be intimately tied to ENSO itself, but capturing an asymmetry in ENSO climate impacts characterized by a phase shift in 500 hPa heights between extreme states of El Niño and La Niña. Consistent with this asymmetry in ENSO teleconnections, we demonstrate that wet conditions occur over far western North America and warm conditions over eastern North America during both strong ENSO phases. The negative phase of the second mode is shown to be an expression of atmospheric responses that occur during ENSO-neutral winters when a distinctive tropical SST pattern having warmth in the far western Pacific and coolness in the far eastern Pacific can arise. This forcing resembles a precursor state that often is followed by a mature El Niño event in 6-9 months. The principal climate impact related to this forced teleconnection is an anomalously dry and warm climate across the western United States.

By comparing the EOF analysis results with those in coupled atmosphere-ocean model simulations forced with observed changes in anthropogenic and natural radiative forcings we found that the third EOF mode is associated with the radiatively forced climate change. This mode explains 6% of the externally forced variance and is thus much weaker than the contribution from first two modes that result from purely internal climate variability. Our analysis reveals that the observed trend of winter heights during the

recent period is more determined by the decadal variability associated with low frequency fluctuations in ENSO than by the external radiative forcing.

Our analysis confirms that there indeed exist additional forced atmospheric response patterns beyond the canonical (linear) ENSO response, supporting the findings of previous studies (e.g. Hoerling and Kumar 2002; Kumar et al. 2005). Our study unravels the physical interpretation of this second mode, and furthermore identifies a third mode of forced responses that is demonstrated to be uniquely related to external radiative forcing. The analysis supports an interpretation that the difference between the two teleconnections of Fig. 1 between 1951-78 versus 1979-2014 is not attributable to emergent forcing related to human-induced climate change. Instead, the difference is most likely symptomatic of different ENSO statistics (two very strong El Niño events) in the recent decades to which the spatial patterns of forced teleconnections are shown herein to be sensitive.

Future work is needed to better understand the predictive value implicit in the knowledge of these forced teleconnections for US climate. For instance, is the potential predictability implied by the three leading teleconnections being realized in current climate prediction systems? What is the contribution of the different modes to US seasonal forecast skill? And, at what lead times are the different forcings of these teleconnections themselves predictable?

Finally, we note that the PC time series of the forced teleconnections describe distinct "forecasts of opportunity". Some are well known, such as the strong El Niño events in 1982-83 and 1997-98. Others are less well known, and deserving additional study. For example, during winter of 2013-14 the negative phase of the second mode was strongly enhanced, an important indicator for a possible role of tropical forcing in that winter and its impact on California precipitation deficits and high temperatures during that winter (see also Seager et al. 2014). Hartmann (2015), using the same model data, also identified a coherent atmospheric teleconnection for 2013-14 that includes a warm West-cold East surface temperature dipole.

APPENDIX A

Comparison of leading modes of variability of 500hPa heights in reanalysis and GFS model simulations

The EOF patterns between the reanalysis data and GFS model simulations are compared to examine the model fidelity in simulating the leading modes of variability of Dec-Feb mean 500hPa heights. Figure A1 (left panels) shows the regression patterns corresponding to the first 3 EOFs of reanalysis data, which explain a combined 54.8% of the wintertime height variability poleward of 20°N. The same EOF procedure is applied to the climate simulations. In this application, we concatenate the individual members of the AMIP simulations, which for the GFS data consist of 1750 winter seasons. Figure A1 (middle panels) shows the regression patterns corresponding to the first 3 EOFs of GFS simulations, which explain a combined 46.8% of the model's wintertime height

variability poleward of 20°N. The model is seen to replicate the leading observed pattern of 500 hPa height variability which consists of a prominent wave train over the Pacific-North American region. The observed second EOF pattern is likewise part of the model's leading modes of variability, though ranked third in its EOF decomposition and explaining less overall height variance. We note that there exists considerable sampling variability in the EOF rankings and detailed structures based on separate samples of only 35 winters (not shown).

The leading patterns of the GFS 500-hPa height variability can be largely reproduced in a climate simulation having no interannual variability in boundary conditions or external radiative forcing. A 100-yr long control integration of GFS has been performed using repeating seasonal cycle SSTs and carbon dioxide concentrations corresponding to the mean of 1979-2014. Figure A1 (right panels) shows the regression patterns corresponding to the first 3 EOFs of this control run, which explain a combined 43.8% of the wintertime height variability poleward of 20°N. The spatial structures are very similar to the AMIP version of the model, and it is evident that internal atmospheric variability is major source of NH wintertime height variability.

APPENDIX B

Comparison of forced modes of variability between GFS and ECHAM4.5 models

The robustness of the boundary forced atmospheric circulation sensitivities shown in Fig. 2 is evaluated by repeating the EOF analysis using different model data. Important in such intercomparison is the use of large-sized ensemble simulations so as not to confound

forced patterns with internal atmospheric variability that may dominate an EOF analysis based on small-sized ensembles. We have therefore used the data from an 85-member ensemble of similarly designed AMIP experiments derived from the ECHAM4.5 model (Roeckner et al. 1996; data provided by IRI, see http://iridl.ldeo.columbia.edu/SOURCES/.IRI/.FD/.ECHAM4p5/.History/.ensemble85/). Differences in parameterizations and spatial resolutions (e.g., ECHAM4.5 is run at T42 scale) permit a meaningful evaluation of whether these large spatial modes of atmospheric sensitivity derived from GFS data are robust to model formulation. Figure B1 compares the height structures corresponding to the first two EOFs of wintertime 500 hPa heights for a common simulation period of 1979-2003. The spatial patterns of the models' corresponding EOFs are very similar (spatial correlation exceeds 0.9 over the map domain), as are the temporal variations in their PC time series (temporal correlation of forced solutions exceeds 0.9 during 1979-2003). This intercomparison reveals that the atmospheric sensitivities do not depend on the selection of a particular model. They are more determined by the nature of the boundary forcing used for each atmospheric model instead.

Acknowledgments

This work was supported by grants from NOAA office of climate programs–the Earth System Science (ESS) Climate Variability and Predictability (CVP) Program. We acknowledge NCAR's CESM1(CAM5) Large Ensemble Community Project for carrying out the large CESM1 ensemble, Xiaowei Quan for carrying out the large CCSM4 ensemble, and Jon Eischeid for his technical support.

References:

An, S-I., and F-F. Jin, 2004: Nonlinearity and asymmetry of ENSO. *J. Climate*, **17,** 2399–2412.

Barnston, A. G., and R. E. Livezey, 1987: Classification, seasonality, and persistence of low-frequency atmospheric circulation patterns. *Mon. Wea. Rev.*, **115,** 1083–1126.

Burgers, G., and D. B. Stephenson, 1999: The "normality" of El Niño. *Geophys. Res. Lett.*, **26,** 1027–1030.

Cane, M. A., 1983: Oceanographic events during El Niño. *Science,* **222,** 1189–1194.

Dommenget, D., T. Bayr, and C. Frauen, 2013: Analysis of the non-linearity in the pattern and time evolution of El Niño Southern Oscillation. *Climate Dyn.*, **40**, 2825–2847.

Geisler, J. E., M. L. Blackmon, G. T. Bates, and S. Munoz, 1985: Sensitivity of January climate response to the magnitude and position of equatorial Pacific sea surface temperature anomalies. *J. Atmos. Sci.*, **42,** 1037–1049.

Gent, P., and Coauthors, 2011: The Community Climate System Model version 4. *J. Climate*, **24**, 4973–4991.

Hartmann, D. L., 2015: Pacific sea surface temperature and the winter of 2014. *Geophys. Res. Lett.,* **42**, doi:10.1002/2015GL063083.

Hoerling, M. P., and A. Kumar, 2000: Understanding and predicting extratropical teleconnections related to ENSO. *El Niño and the Southern Oscillation: Multi-Scale Variability, and Global and Regional Impacts,* H. Diaz and V. Markgraf, Eds., Cambridge University Press, 57–88.

Hoerling, M. P., and A. Kumar, 1997: Origins of extreme climate states during the 1982-83 ENSO winter. *J. Climate*, **10**, 2859-2870.

Hoerling, M. P., and A. Kumar, 2002: Atmospheric response patterns associated with tropical forcing. *J. Climate*, **15,** 2184–2203.

Hoerling, M. P., A. Kumar, and M. Zhong, 1997: El Niño, La Niña, and the nonlinearity of their teleconnections. *J. Climate*, **10,** 1769–1786.

Hoerling, M. P., A. Kumar, and T.-Y. Xu, 2001: Robustness of the nonlinear atmospheric response to opposite phases of ENSO. *J. Climate*, **14**, 1277-1293.

Horel J. D. and J. M. Wallace, 1981: Planetary-Scale Atmospheric Phenomena Associated with the Southern Oscillation. *Mon. Wea. Rev.*, **109**, 813–829.

Hoskins, B. J., and D. J. Karoly, 1981: The steady linear response of a spherical atmosphere to thermal and orographic forcing. *J. Atmos. Sci.*, **38,** 1179–1196.

Hurrell, J., J. Hack, D. Shea, J. Caron, and J. Rosinski, 2008: A new sea surface temperature and sea ice boundary data set for the Community Atmosphere Model. *J. Climate*, **21**, 5145–5153.

IPCC, 2013: Climate Change 2013: The Physical Science Basis. Contribution of Working Group I to the Fifth Assessment Report of the Intergovernmental Panel on Climate Change [Stocker, T.F., D. Qin, G.-K. Plattner, M. Tignor, S.K. Allen, J. Boschung, A. Nauels, Y. Xia, V. Bex and P.M. Midgley (eds.)]. Cambridge University Press, Cambridge, United Kingdom and New York, NY, USA, 1535 pp, doi:10.1017/CBO9781107415324.

Kalnay, E., et al., 1996: The NCEP/NCAR 40-year reanalysis project, *Bull. Am. Meteorol. Soc.*, **77**, 437–471.

Kang, I. S, and Coauthors, 2002: Intercomparison of Atmospheric GCM Simulated Anomalies Associated with the 1997/98 El Niño. *J. Climate*, **15**, 2791–2805.

Kay, J. E., Deser, C., Phillips, A., Mai, A., Hannay, C., Strand, G., Arblaster, J., Bates, S., Danabasoglu, G., Edwards, J., Holland, M. Kushner, P., Lamarque, J.-F., Lawrence, D., Lindsay, K., Middleton, A., Munoz, E., Neale, R., Oleson, K., Polvani, L., and M. Vertenstein, 2015: The Community Earth System Model (CESM) Large Ensemble Project: A Community Resource for Studying Climate Change in the Presence of Internal Climate Variability, *Bulletin of the American Meteorological Society*, doi:10.1175/BAMS-D-13-00255.1 (in press)

Kumar, A., Q. Zhang, P. Peng, and B. Jha, 2005: SST-Forced Atmospheric Variability in an Atmospheric General Circulation Model. *J. Climate*, **18**, 3953–3967.

Mantua, N. J., S. R. Hare, Y. Zhang, J. Wallace, and R. C. Francis, 1997: A Pacific interdecadal climate oscillation with impacts on salmon production. *Bull. Amer. Meteor. Soc.*, **78,** 1069–1079.

Meehl, G. A., and Coauthors, 2013: Climate change projections in CESM1 (CAM5) compared to CCSM4. *J. Climate*, **26**, 6287–6308, doi:10.1175/JCLI-D-12-00572.1.

Mo, K. C. and R. E. Livezey, 1986: Tropical-Extratropical Geopotential Height Teleconnections during the Northern Hemisphere Winter. *Mon. Wea. Rev.*, **114**, 2488–2515.

Neale, R. B., and Coauthors, 2010: Description of the NCAR Community Atmosphere Model (CAM 4.0). NCAR Tech. Note NCAR/TN-485+STR, 212 pp.

Neale, R. B., and Coauthors, 2012: Description of the NCAR Community Atmosphere Model (CAM 5.0). NCAR Tech. Note NCAR/TN-486+STR, 274 pp.

Palmer, T. N., and D. A. Mansfield, 1986a: A study of wintertime circulation anomalies during past El Niño events using a high resolution general circulation model: I: Influence of model climatology. *Quart. J. Roy. Meteor. Soc.*, **112,** 613–638.

Palmer, T. N., and D. A. Mansfield, 1986b: A study of wintertime circulation anomalies during past El Niño events using a high resolution general circulation model: II: Variability of the seasonal mean response. *Quart. J. Roy. Meteor. Soc.*, **112,** 639–660.

Penland, C., and P. D. Sardeshmukh, 1995: The optimal growth of tropical sea surface temperature anomalies. *J. Climate*, **8,** 1999–2024.

Perlwitz, J., M. P. Hoerling, and R. Dole, 2015: Arctic Tropospheric Warming: Causes and Linkages to Lower Latitudes. *J. Climate*, **28**, 2154–2167. doi: http://dx.doi.org/10.1175/JCLI-D-14-00095.1

Rasmusson, E. M., and J. M. Wallace, 1983: Meteorological aspects of the El Niño/Southern Oscillation. *Science,* **222,** 1195–1202.

Roeckner, E., and Coauthors, 1996: The atmospheric general circulation model ECHAM4: Model description and simulation of present-day climate. Max-Planck-Institut fur Meteorologie Rep. 218, Hamburg, Germany, 90 pp.

Saha, S., and Coauthors, 2014: The NCEP Climate Forecast System version 2. *J. Climate*, **27**, 2185–2208, doi:10.1175/JCLI-D-12-00823.1.

Seager, R., M. Hoerling, S. Schubert, H. Wang, B. Lyon, A. Kumar, J. Nakamura, and N. Henderson; 2014: Causes and predictability of the 2011-14 California drought. Report of the NOAA Drought Task Force, doi:10.7289/V58K771F, 40 pp., [Available at *http://docs.lib.noaa.gov/noaa_documents/OAR/CPO/MAPP/california_drought_2011-2014.pdf]*

Simmons, A. J., 1982: The forcing of stationary wave motions by tropical diabatic forcing. *Quart. J. Roy. Meteor. Soc.*, **108,** 503–534.

Simmons, A. J., J. M. Wallace, and G. Branstator, 1983: Barotropic wave propagation and instability, and atmospheric teleconnection patterns. *J. Atmos. Sci.*, **40,** 1363–1392.

Ting, M., and P. D. Sardeshmukh, 1993: Factors determining the extratropical response to equatorial diabatic heating anomalies. J. *Atmos. Sci.* , **50**, 907-918.

Trenberth, K. E., and D. P. Stepaniak, 2001: Indices of El Niño Evolution. *J. Climate*, **14**, 1697–1701.

Wang, S.-Y., L. Hipps, R. R. Gillies, *and* J.-H. Yoon, 2014*:* Probable causes of the abnormal ridge accompanying the 2013–2014 California drought: ENSO precursor and anthropogenic warming footprint, *Geophys. Res. Lett.,* **41**, 3220–3226, *doi:*10.1002/2014GL059748.

Zhang, T., D.-Z. Sun, R. Neale, and P. J. Rasch, 2009: An evaluation of ENSO asymmetry in the Community Climate System Models: A view from the subsurface. *J. Climate*, **22**, 5933–5961.

Zhang, T., J. Perlwitz, and M. P. Hoerling, 2014: What is responsible for the strong observed asymmetry in teleconnections between El Niño and La Niña? *Geophys. Res. Lett.*, **41**, 1019–1025, doi:10.1002/2013GL058964.

Zhang, T., and D.-Z. Sun, 2014: ENSO Asymmetry in CMIP5 Models. *J. Climate*, **27**, 4070-4093, doi:10.1175/JCLI-D-13-00454.1.

Zhang, Y., J. M. Wallace, and D. S. Battisti, 1997: ENSO-like interdecadal variability: 1900–1993. *J. Climate*, **10,** 1004–1020.

Figure Captions

Figure 1. The observed regression pattern of winter (DJF) season 500-hPa heights onto the Niño3.4 SST anomalies over the 20°N-90°N domain for (top) the period of 1951-1978 and (bottom) the period of 1979-2014. The height field from NCEP reanalysis and Hurrell SST data (Hurrell et al. 2008) are used in the calculation. The contour interval is 5 meter per degree.

Figure 2. (left) The spatial pattern and (right) PC time series of the leading two EOFs of GFSv2 simulated 50-member ensemble mean winter (DJF) season 500-hPa heights. The analysis is computed over the 20°N-90°N domain for 1979/80 through 2013/14. The ordinate of the PC time series is of the standardized departure. The EOF patterns are shown as the regressions of the heights onto the PC time series, and drawn at the interval of 5 meter for a 1 standardized departure of PC index.

Figure 3. The scatter relationship between tropical Pacific SST indices and the PC indices shown in Figure 2. The top panel shows the relationship between N3.4 (SST anomalies in the Niño 3.4 region) standardized index and PC1 index, and the bottom panel shows the relationship between TNI (Trans-Niño Index) standardized index and PC2 index.

Figure 4. The scatter relationship between PC1 index and PC2 index shown in Figure 2.

Figure 5. (left) The composite DJF anomalies of (first row) Northern Hemisphere 500-hPa height, (second row) tropical SST, (third row) North American surface temperature,

(fourth row) tropical precipitation, and (fifth row) North American precipitation for 7 strongest cases with positive PC1 values shown in Figure 4. (right) Corresponding anomalies for 7 strongest cases with negative PC1 values shown in Figure 4. The contour interval of height is 10 meter (first row).

Figure 6. The sum between composite DJF anomalies of 7 strongest cases with positive PC1 values (left panels of Figure 5) and composite DJF anomalies of 7 strongest cases with negative PC1 values (right panels of Figure 5). The contour interval of height is 10 meter (first row).

Figure 7. (left) The composite DJF anomalies of (first row) Northern Hemisphere 500-hPa height, (second row) tropical SST, (third row) North American surface temperature, (fourth row) tropical precipitation, and (fifth row) North American precipitation for 7 strongest cases with positive PC2 values shown in Figure 4. (right) Corresponding anomalies for 7 strongest cases with negative PC2 values shown in Figure 4. The contour interval of height is 10 meter (first row).

Figure 8. Top panels show (left) the spatial pattern and (right) PC time series of EOF3 of GFSv2 simulated 50-member ensemble mean winter (DJF) season 500-hPa heights. The bottom panels show (left) the spatial pattern and (right) PC time series of the leading EOF of 50-member ensemble mean winter (DJF) season 500-hPa heights in coupled model runs which include 20 runs from CCSM4 and 30 runs from CESM1. The analysis is computed over the 20°N-90°N domain for 1979/80 through 2013/14. The ordinate of

the PC time series is of the standardized departure. The EOF patterns are shown as the regressions of the heights onto the PC time series, and drawn at the interval of 1 meter for a 1 standardized departure of PC index.

Figure 9. (Top) The ratio of forced component to the total variance of winter (DJF) seasonally averaged 500-hPa height for 1979/80 through 2013/14 in GFSv2 AMIP runs. The results are shown for (left) the NH polar cap to 20°N, and for (right) the global domain. (Bottom) corresponding results from coupled model runs which are the combinations of the runs from CCSM4 and CESM1. The contour interval is 0.05 for left panels and 0.2 for right panels. Forced variability is computed from the variance of ensemble means. Total variability is computed from the concatenated time series of the individual members. For two coupled models, the total variability is computed for each separately, and then averaged.

Figure 10. The ratio of the leading three EOFs of forced component to the total variance of winter (DJF) seasonally averaged 500-hPa height for 1979/80 through 2013/14 in GFSv2 AMIP runs. The height anomalies projecting on different modes can be computed as the scalar product of different EOF patterns and the associated PC time series. The contour interval is 0.05 in three panels of the figure.

Figure 11. The trend pattern of EOF1, the sum of EOF1 and EOF3, and the trend of ensemble mean of winter (DJF) season 500-hPa heights from GFSv2 AMIP runs over the 20°N-90°N domain for 1979/80 through 2013/14. The observed trend pattern is shown in

lower left. The trend patterns of EOF1 and EOF3 are obtained by the product between the EOF pattern and the total trend of the corresponding PC time series (the total trend is -1.09 for PC1 and 2.0 for PC3) shown in the top panels of Figure 2 and Figure 8, respectively. The contour interval is 5 meter in four panels of the figure.

Figure A1. The spatial pattern of the leading three EOFs of winter (DJF) season 500-hPa heights from (left) observations, (middle) the concatenation of all 50 AMIP runs of GFSv2 and (right) a 100-yr-long GFSv2 control run in which the model is driven by observed SST climatology. The observational estimate is based on NCEP reanalysis for 1979/80 through 2013/14. The analysis is computed over the 20°N-90°N domain. The EOF patterns are shown as the regressions of the heights onto the standardized PC time series, and drawn at the interval of 5 meter for a 1 standardized departure of PC index.

Figure B1. (left) The spatial pattern and (right) PC time series of the leading two EOFs of winter (DJF) season 500-hPa heights from GFSv2 AMIP runs and ECHAM4.5 AMIP runs for the common period of 1979-2003. The analysis is computed over the 20°N-90°N domain based on 50-member ensemble mean from GFSv2 model and 85-member ensemble mean from ECHAM4.5 model. The ordinate of the PC time series is of the standardized departure. The EOF patterns are shown as the regressions of the heights onto the PC time series, and drawn at the interval of 5 meter for a 1 standardized departure of PC index.

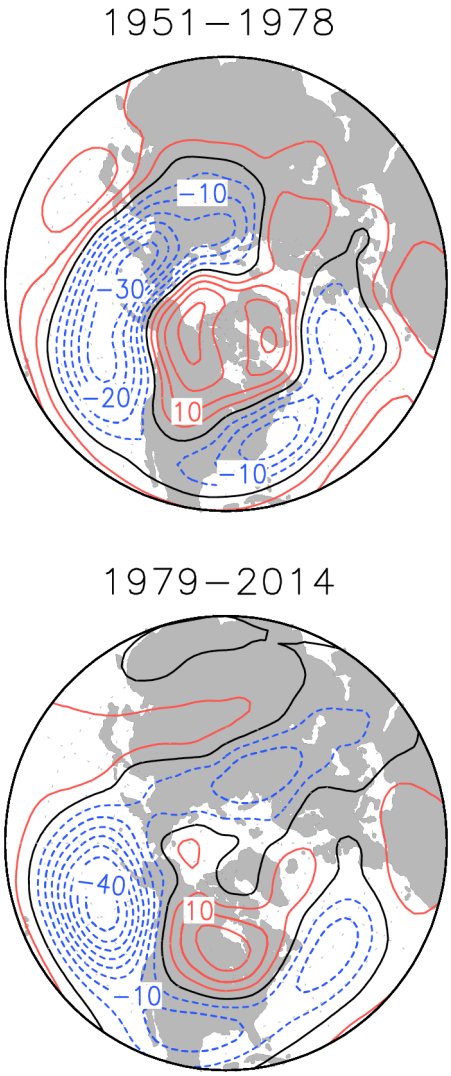

Figure 1. The observed regression pattern of winter (DJF) season 500-hPa heights onto the Niño3.4 SST anomalies over the 20°N-90°N domain for (top) the period of 1951-1978 and (bottom) the period of 1979-2014. The height field from NCEP reanalysis and Hurrell SST data (Hurrell et al. 2008) are used in the calculation. The contour interval is 5 meter per degree.

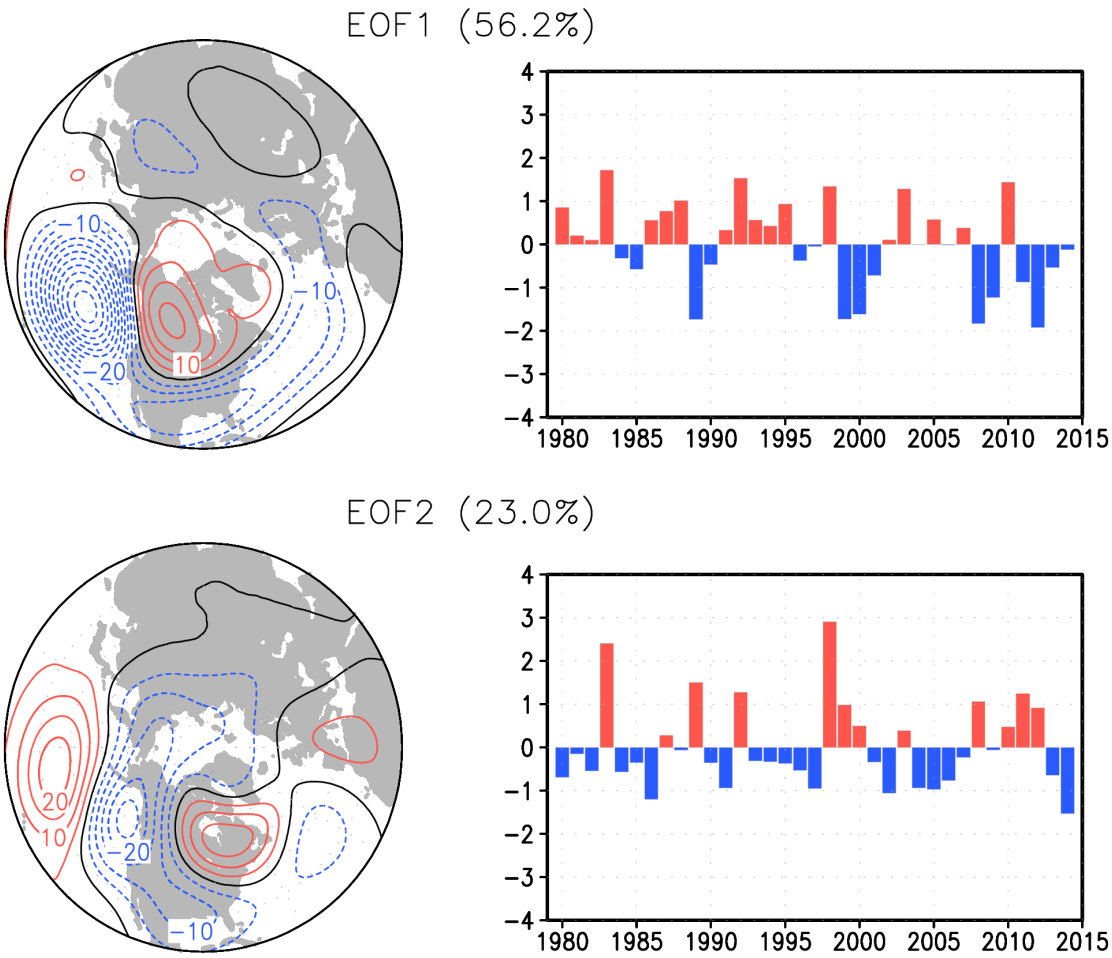

Figure 2. (left) The spatial pattern and (right) PC time series of the leading two EOFs of GFSv2 simulated 50-member ensemble mean winter (DJF) season 500-hPa heights. The analysis is computed over the 20°N-90°N domain for 1979/80 through 2013/14. The ordinate of the PC time series is of the standardized departure. The EOF patterns are shown as the regressions of the heights onto the PC time series, and drawn at the interval of 5 meter for a 1 standardized departure of PC index.

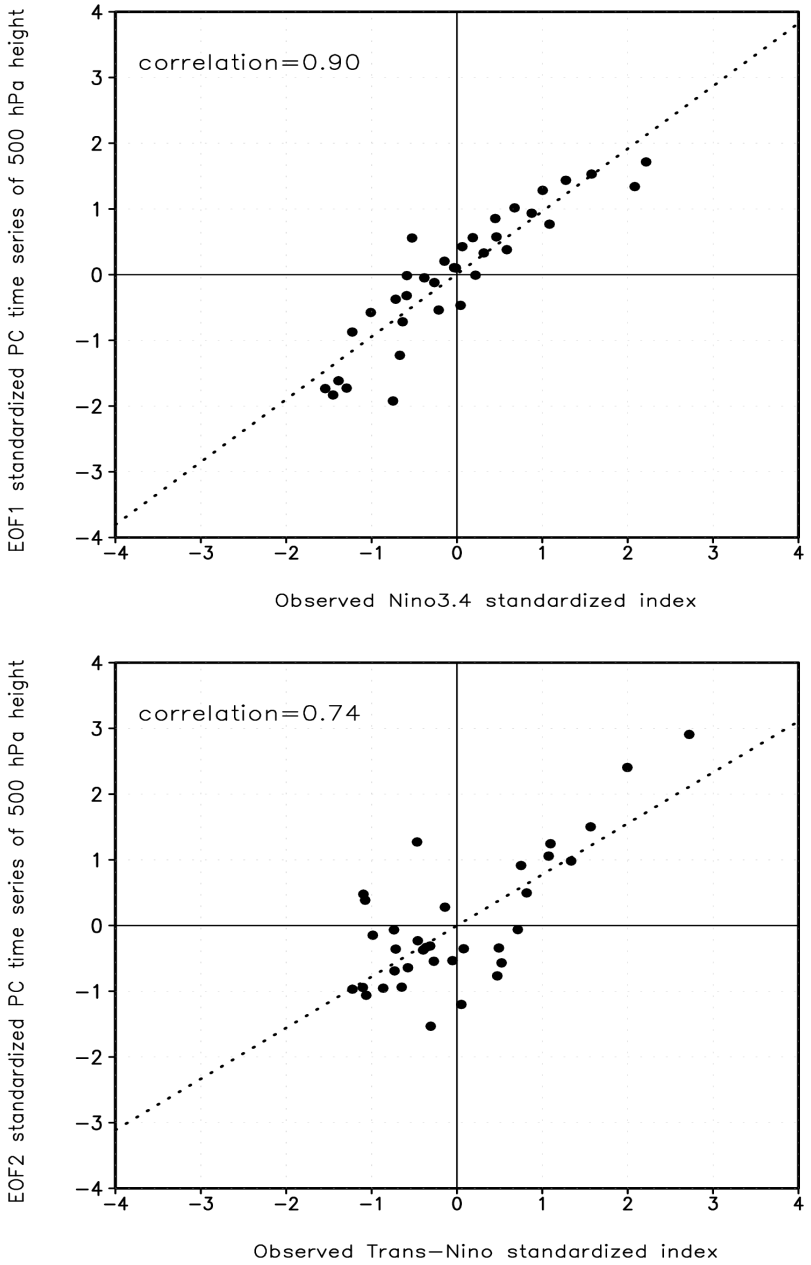

Figure 3. The scatter relationship between tropical Pacific SST indices and the PC indices shown in Figure 2. The top panel shows the relationship between N3.4 (SST anomalies in the Niño 3.4 region) standardized index and PC1 index, and the bottom panel shows the relationship between TNI (Trans-Niño Index) standardized index and PC2 index.

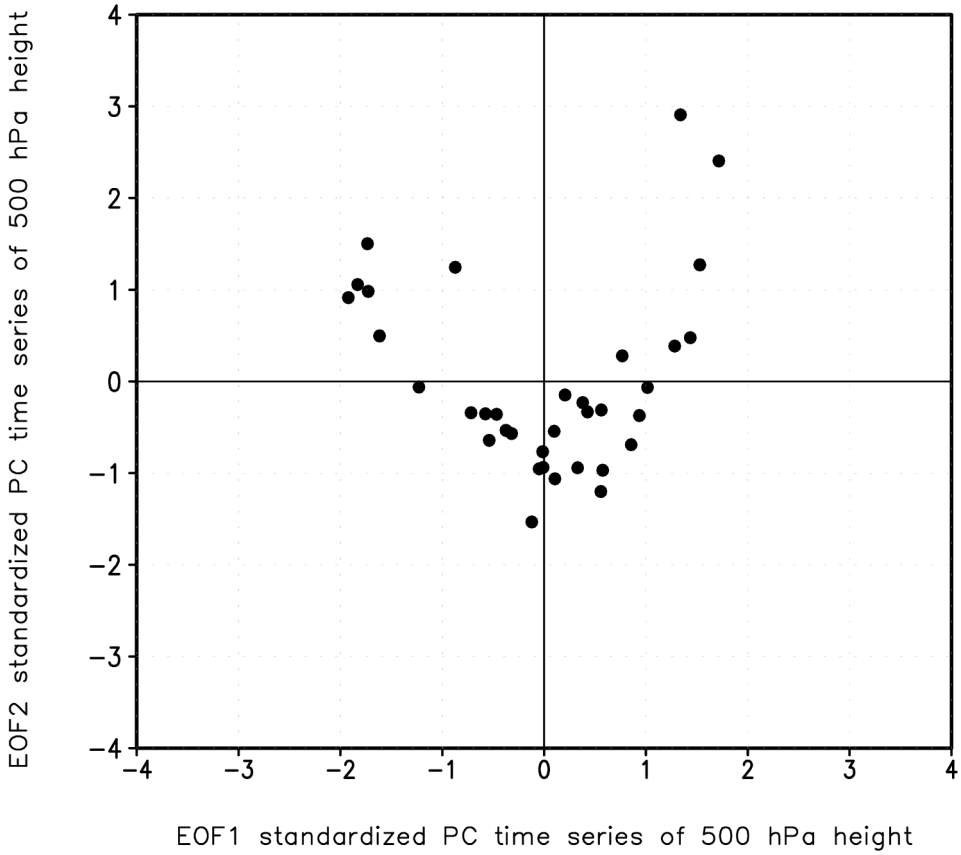

Figure 4. The scatter relationship between PC1 index and PC2 index shown in Figure 2.

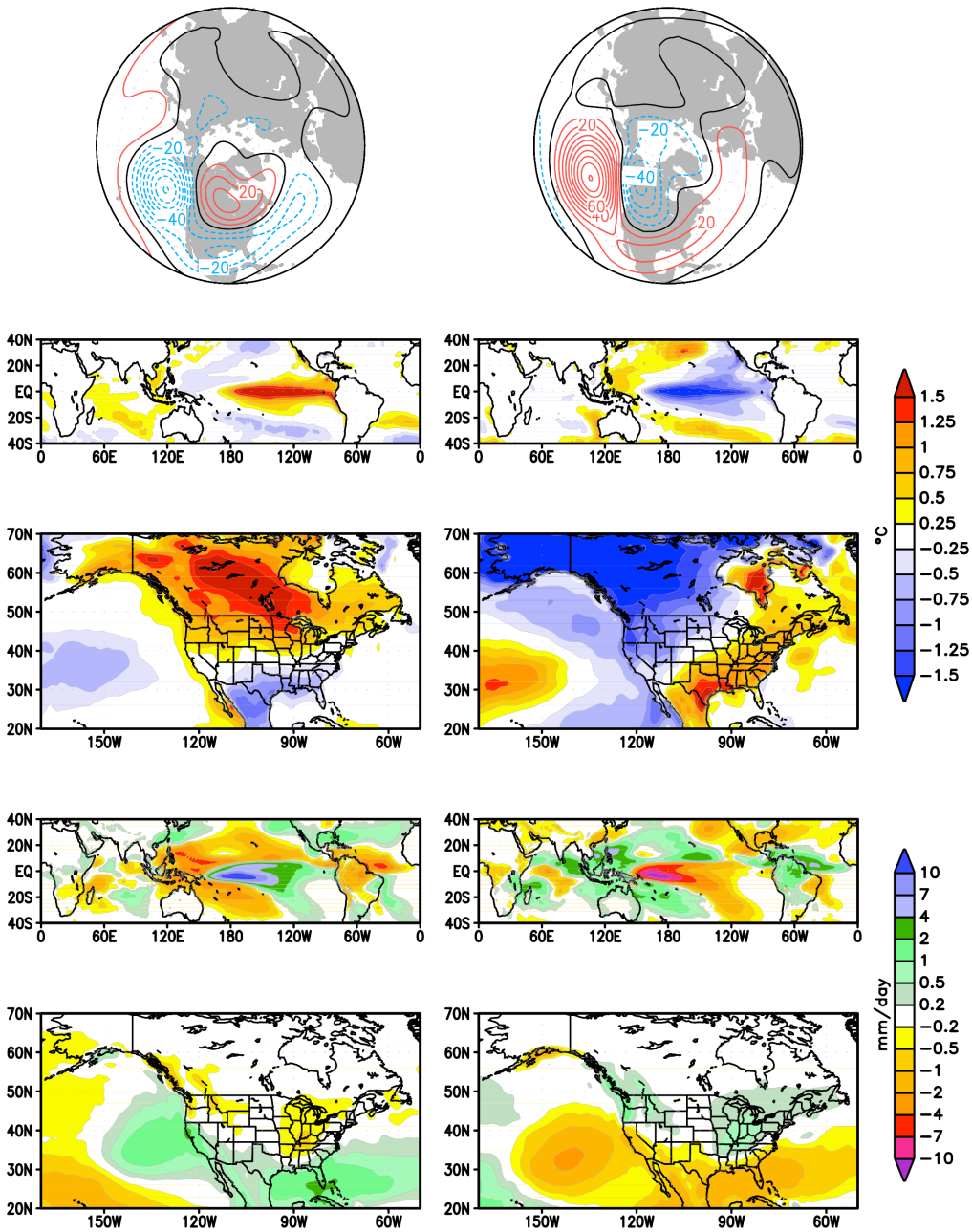

Figure 5. (left) The composite DJF anomalies of (first row) Northern Hemisphere 500-hPa height, (second row) tropical SST, (third row) North American surface temperature, (fourth row) tropical precipitation, and (fifth row) North American precipitation for 7 strongest cases with positive PC1 values shown in Figure 4. (right) Corresponding anomalies for 7 strongest cases with negative PC1 values shown in Figure 4. The contour interval of height is 10 meter (first row).

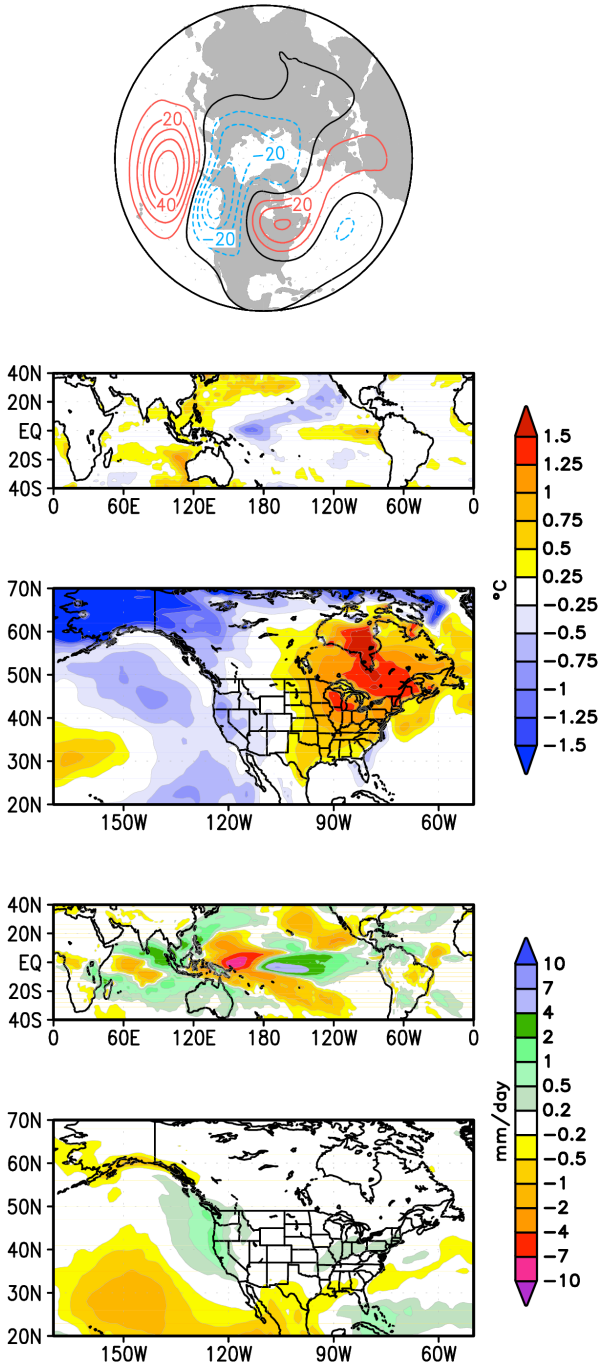

Figure 6. The sum between composite DJF anomalies of 7 strongest cases with positive PC1 values (left panels of Figure 5) and composite DJF anomalies of 7 strongest cases with negative PC1 values (right panels of Figure 5). The contour interval of height is 10 meter (first row).

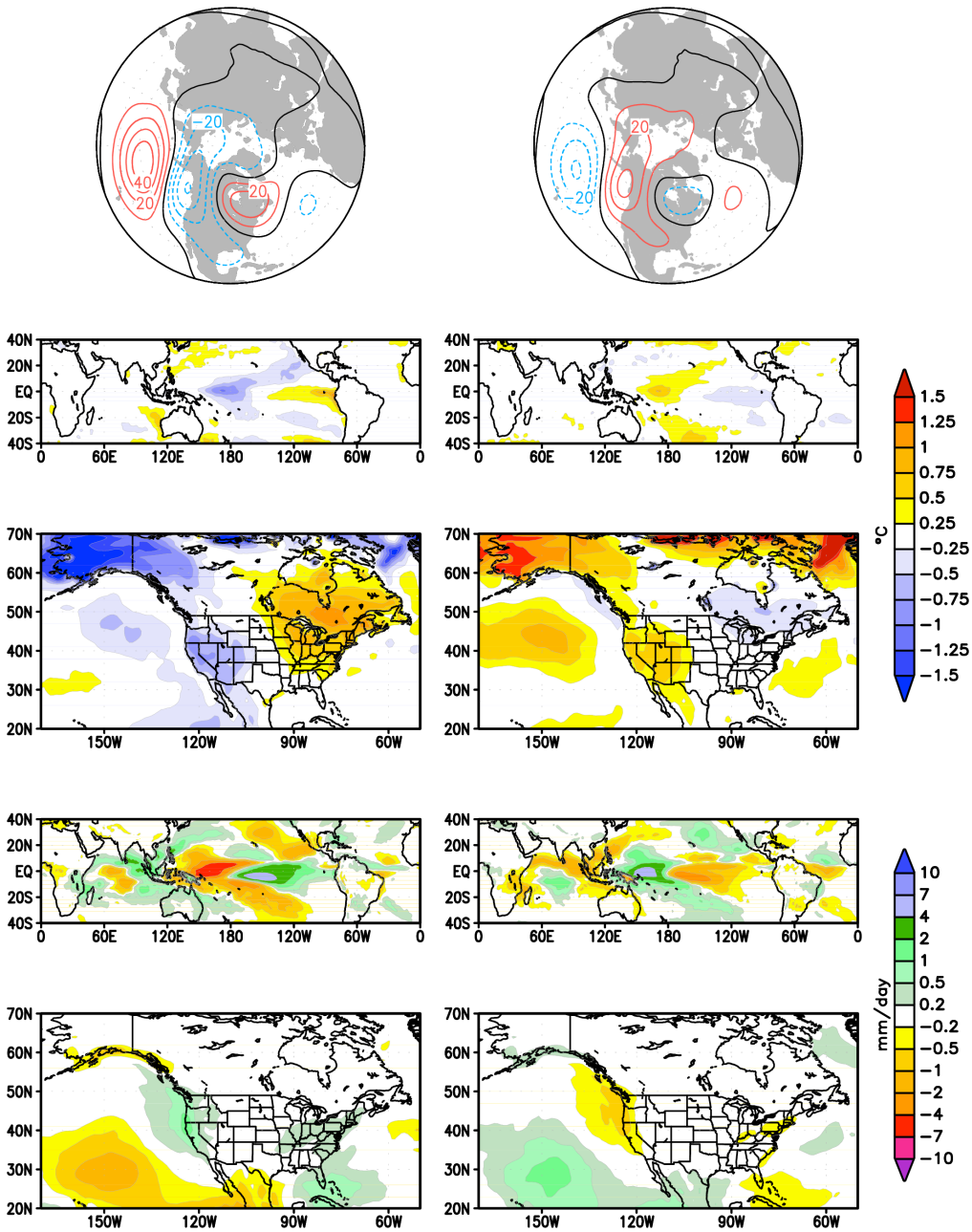

Figure 7. (left) The composite DJF anomalies of (first row) Northern Hemisphere 500-hPa height, (second row) tropical SST, (third row) North American surface temperature, (fourth row) tropical precipitation, and (fifth row) North American precipitation for 7 strongest cases with positive PC2 values shown in Figure 4. (right) Corresponding anomalies for 7 strongest cases with negative PC2 values shown in Figure 4. The contour interval of height is 10 meter (first row).

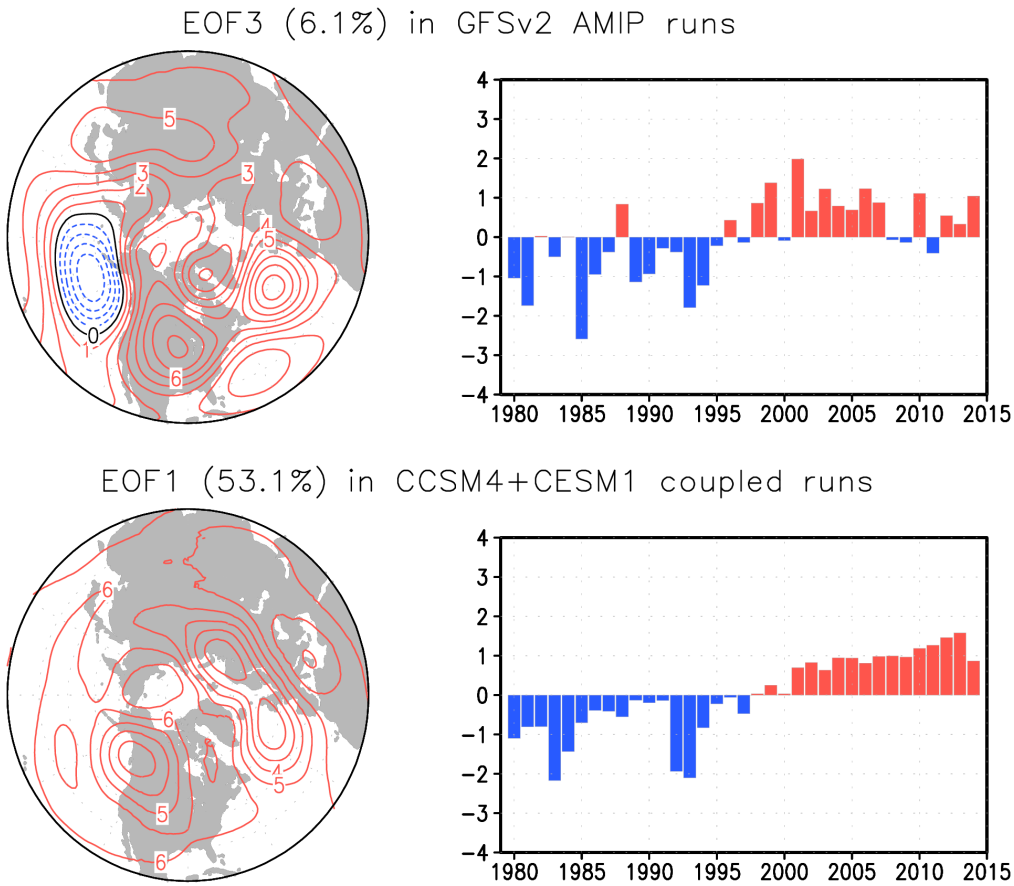

Figure 8. Top panels show (left) the spatial pattern and (right) PC time series of EOF3 of GFSv2 simulated 50-member ensemble mean winter (DJF) season 500-hPa heights. The bottom panels show (left) the spatial pattern and (right) PC time series of the leading EOF of 50-member ensemble mean winter (DJF) season 500-hPa heights in coupled model runs which include 20 runs from CCSM4 and 30 runs from CESM1. The analysis is computed over the 20°N-90°N domain for 1979/80 through 2013/14. The ordinate of the PC time series is of the standardized departure. The EOF patterns are shown as the regressions of the heights onto the PC time series, and drawn at the interval of 1 meter for a 1 standardized departure of PC index.

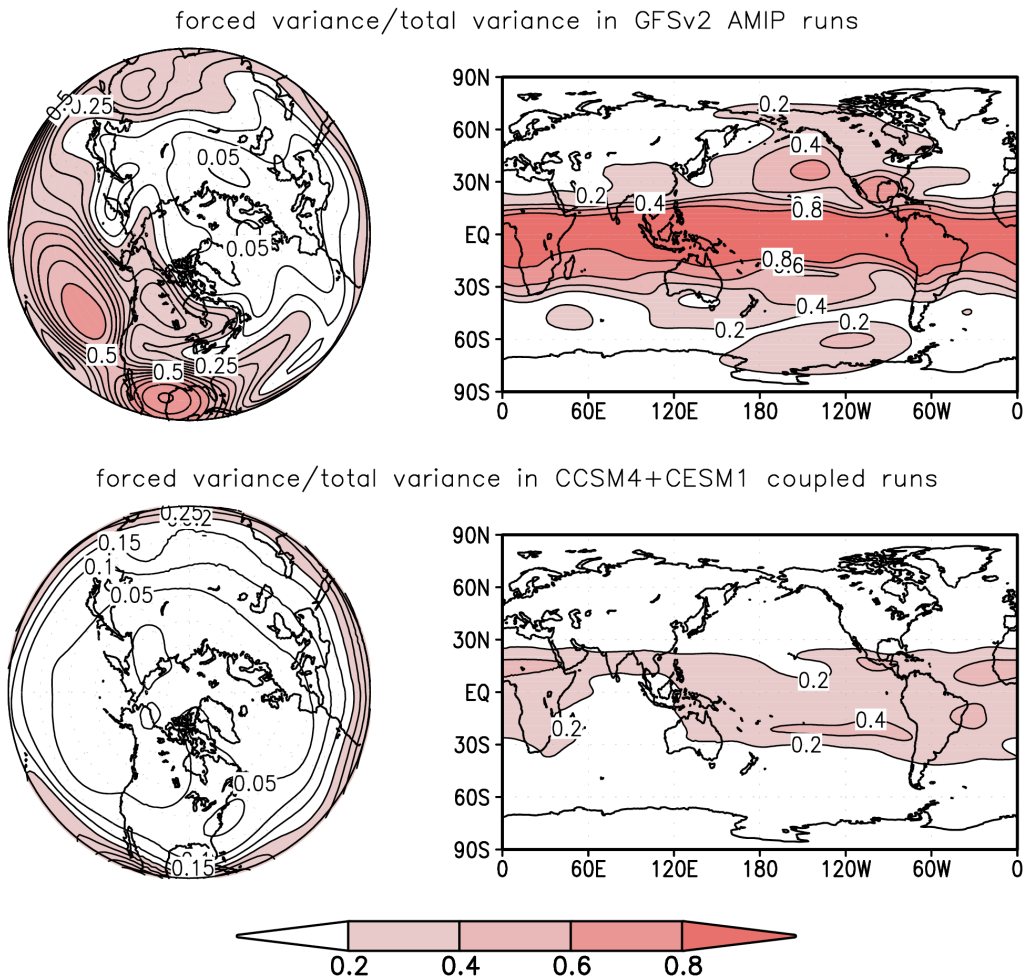

Figure 9. (Top) The ratio of forced component to the total variance of winter (DJF) seasonally averaged 500-hPa height for 1979/80 through 2013/14 in GFSv2 AMIP runs. The results are shown for (left) the NH polar cap to 20°N, and for (right) the global domain. (Bottom) corresponding results from coupled model runs which are the combinations of the runs from CCSM4 and CESM1. The contour interval is 0.05 for left panels and 0.2 for right panels. Forced variability is computed from the variance of ensemble means. Total variability is computed from the concatenated time series of the individual members. For two coupled models, the total variability is computed for each separately, and then averaged.

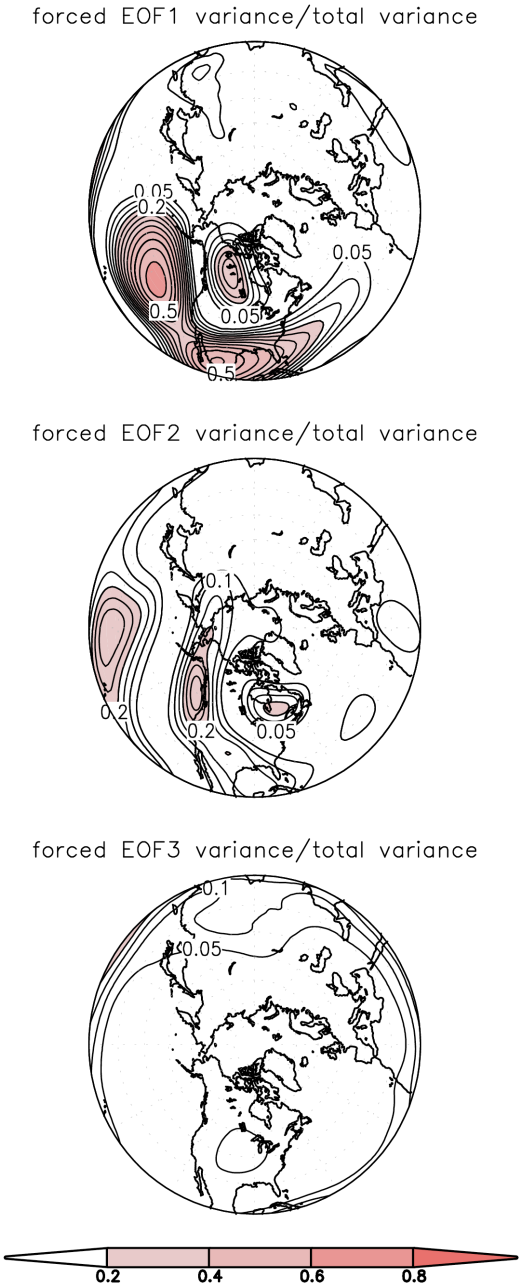

Figure 10. The ratio of the leading three EOFs of forced component to the total variance of winter (DJF) seasonally averaged 500-hPa height for 1979/80 through 2013/14 in GFSv2 AMIP runs. The height anomalies projecting on different modes can be computed as the scalar product of different EOF patterns and the associated PC time series. The contour interval is 0.05 in three panels of the figure.

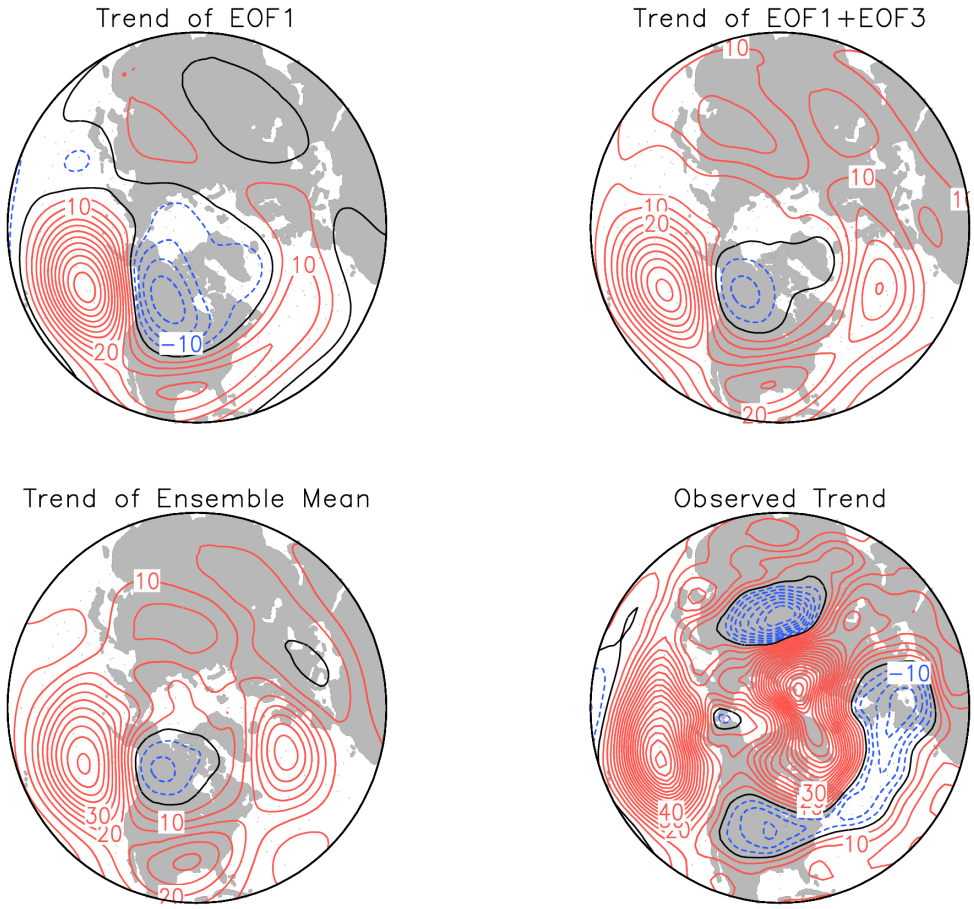

Figure 11. The trend pattern of EOF1, the sum of EOF1 and EOF3, and the trend of ensemble mean of winter (DJF) season 500-hPa heights from GFSv2 AMIP runs over the 20°N-90°N domain for 1979/80 through 2013/14. The observed trend pattern is shown in lower left. The trend patterns of EOF1 and EOF3 are obtained by the product between the EOF pattern and the total trend of the corresponding PC time series (the total trend is -1.09 for PC1 and 2.0 for PC3) shown in the top panels of Figure 2 and Figure 8, respectively. The contour interval is 5 meter in four panels of the figure.

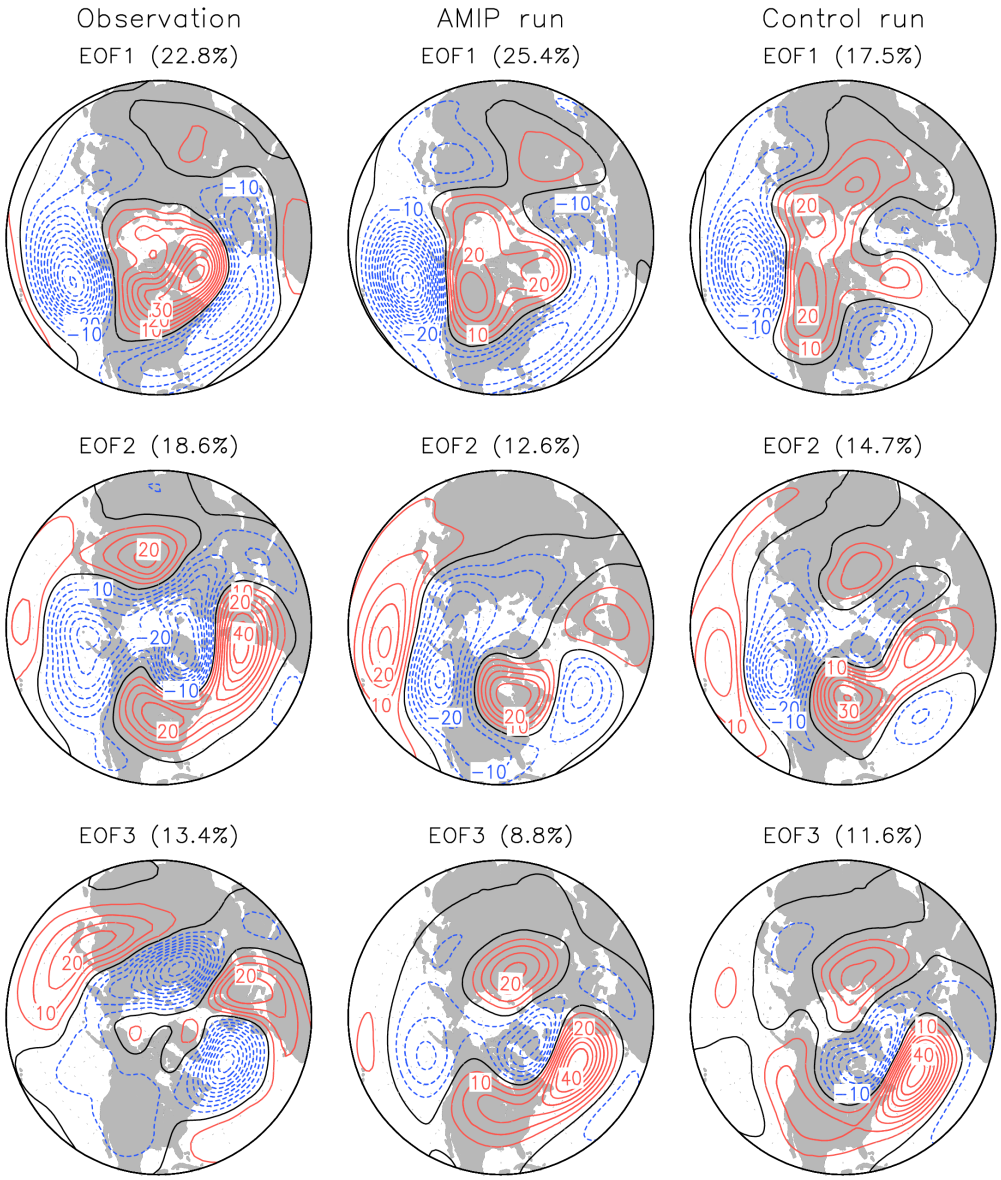

Figure A1. The spatial pattern of the leading three EOFs of winter (DJF) season 500-hPa heights from (left) observations, (middle) the concatenation of all 50 AMIP runs of GFSv2 and (right) a 100-yr-long GFSv2 control run in which the model is driven by observed SST climatology. The observational estimate is based on NCEP reanalysis for 1979/80 through 2013/14. The analysis is computed over the 20°N-90°N domain. The EOF patterns are shown as the regressions of the heights onto the standardized PC time series, and drawn at the interval of 5 meter for a 1 standardized departure of PC index.

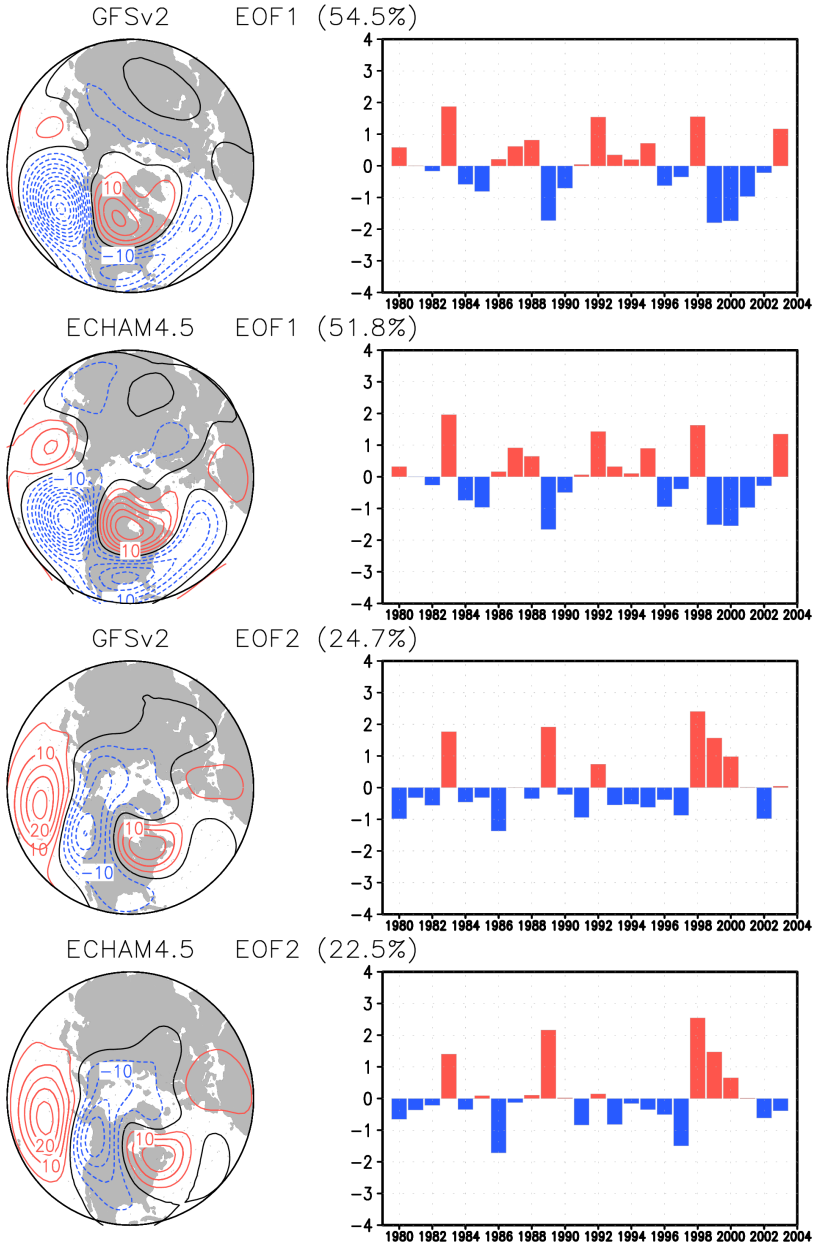

Figure B1. (left) The spatial pattern and (right) PC time series of the leading two EOFs of winter (DJF) season 500-hPa heights from GFSv2 AMIP runs and ECHAM4.5 AMIP runs for the common period of 1979-2003. The analysis is computed over the 20°N-90°N domain based on 50-member ensemble mean from GFSv2 model and 85-member ensemble mean from ECHAM4.5 model. The ordinate of the PC time series is of the standardized departure. The EOF patterns are shown as the regressions of the heights onto the PC time series, and drawn at the interval of 5 meter for a 1 standardized departure of PC index.